BMC Medical Imaging

RESEARCH Open Access

Deep learning-based CT-free attenuation correction for cardiac SPECT: a new approach

Pei Yang[1†], Zeao Zhang[2†], Jianan Wei[2], Lisha Jiang[1], Liqian Yu[1], Huawei Cai[1], Lin Li[1], Quan Guo[2,3*] and Zhen Zhao[1*]

Abstract

Background Computed tomography attenuation correction (CTAC) is commonly used in cardiac SPECT imaging to reduce soft-tissue attenuation artifacts. However, CTAC is prone to inaccuracies due to CT artifacts and SPECT-CT mismatch, along with additional radiation exposure to patients. Thus, these limitations have led to increasing interest in CT-free AC, with deep learning (DL) offering promising solutions. We proposed a new DL-based CT-free AC methods for cardiac SPECT.

Methods We developed a feature alignment attenuation correction network (FA-ACNet) based on the 3D U-Net framework to generate predicted DL-based AC SPECT (Deep AC). The network was trained on 167 cardiac SPECT/CT studies using 5-fold cross validation and tested in an independent testing set ($n=35$), with CTAC serving as the reference. During training, multi-scale features from non-attenuation-corrected (NAC) SPECT and CT were processed separately and then aligned with the encoded features from NAC SPECT using adversarial learning and distance metric learning techniques. The performance of FA-ACNet was evaluated using mean square error (MSE), structural similarity index (SSIM) and peak signal-to-noise ratio (PSNR). Additionally, semi-quantitative evaluation of Deep AC images was performed and compared to CTAC using Bland-Altman plots.

Results FA-ACNet achieved an MSE of $16.94 \pm 2.03 \times 10^{-6}$, SSIM of 0.9955 ± 0.0006 and PSNR of 43.73 ± 0.50 after 5-fold cross validation. Compared to U-Net, MSE and PSNR improved by aligning multi-scale features from NAC SPECT and CT with those from NAC SPECT. In the testing set, FA-ACNet achieved an MSE of 11.98×10^{-6}, SSIM of 0.9976 and PSNR of 45.54. The 95% limits of agreement (LoAs) between the Deep AC and CTAC images for the summed stress/rest scores (SSS/SRS) were [− 2.3, 2.8] and [-1.9,2.1] in the training set and testing set respectively. Changes in perfusion categories were observed in 4.19% and 5.9% of studies assessed for global perfusion scores in the training set and testing set.

Conclusion We propose a novel DL-based CT-free AC approach for cardiac SPECT, which can generate AC images without the need for a CT scan. By leveraging multi-scale features from both NAC SPECT and CT, the performance of CT-free AC is significantly enhanced, offering a promising alternative for future DL-based AC strategies.

Keywords Deep learning, SPECT, Myocardial perfusion imaging, Attenuation correction

†Pei Yang and Zeao Zhang contributed equally to this work.

*Correspondence:
Quan Guo
guoquan@scu.edu.cn
Zhen Zhao
zhaozhen1982@126.com

[1]Department of Nuclear Medicine, West China Hospital of Sichuan University, No.37 Guo Xue Alley, Chengdu 610041, China
[2]Machine Intelligence Laboratory, College of Computer Science, Sichuan University, No. 24 South Section 1, Yihuan Road, Chengdu 610065, China
[3]College of Artificial Intelligence, Guangxi Minzu University, China

Background

Myocardial perfusion imaging (MPI) by single-photon emission computed tomography (SPECT) is an extensively used non-invasive imaging approach for diagnosing and assessing treatment outcomes in obstructive coronary artery disease (CAD) [1–4]. In the clinical practice, detection of regional perfusion abnormalities in MPI can identify high-risk patients with obstructive CAD. However, the imaging appearance of perfusion abnormalities may mimic soft-tissue attenuation artifacts, particularly those caused by the diaphragm, breast tissue, or obesity [5–7]. These soft-tissue attenuation artifacts may cause false-positive results, leading to unnecessary invasive coronary angiography (ICA) or overtreatment.

Attenuation correction (AC) is a critical technique used to compensate for the impact of varying tissue densities on the gamma rays emitted from a radioactive tracer. It helps to mitigate soft-tissue attenuation artifacts by applying mathematical algorithms that estimate the degree of attenuation based on the patient's anatomical information. By compensating for the attenuation effects, AC could reduce soft-tissue attenuation artifacts and improve the diagnostic accuracy of cardiac SPECT [8]. Computed tomography attenuation correction (CTAC) is a commonly used method for cardiac SPECT that converts Hounsfield units from CT scans into attenuation coefficients [9, 10]. However, CTAC approaches may still introduce artifacts, primarily due to CT-related issues [11] and SPECT-CT mismatches [12–14]. Moreover, the use of CT scans also increases additional radiation exposure to patients. Thus, there is an important need to develop CT-free AC methods for SPECT.

Recently, deep learning (DL) has shown promising results in medical image classification [15], image segmentation [16], and image generation [17]. DL-based AC methods have been proposed to generate predicted AC SPECT images (Deep AC) without the need for a CT scan [18]. There are two main strategies for DL-based AC in cardiac SPECT including direct and indirect method. The direct methods involve predicting Deep AC directly from non-attenuation-corrected (NAC) SPECT images [19–21], while the indirect methods focus on predicting synthetic attenuation maps, which can be incorporated into iterative reconstructions for AC or implemented in a vendor-independent post-reconstruction manner [22, 23]. These methods have shown promise to CT-free AC task. However, the direct methods seem to rely on correlation between the NAC and CTAC and the indirect methods focus on the NAC and attenuation map. The additional anatomical and attenuation information provided by raw CT images is often underutilized in both methods. The potential for the information contained in CT images to enhance the correlation of NAC images and CTAC images remains unclear. Thus, we investigated whether incorporating additional CT images could enhance DL-based CT-free AC for cardiac SPECT.

In this study, we propose a novel CT-free AC approach for cardiac SPECT based on a 3D U-Net framework to leverage additional CT images and enhance CT-free AC performance, and evaluated this model on a dataset of 202 clinical stress/rest cardiac SPECT images.

Methods

Cardiac SPECT/CT datasets

This retrospective study was approved by the local institutional review board and the requirement for informed consent was waived (approval number: 20231386). We collected 202 anonymized myocardial perfusion studies that used ^{99m}Tc-sestamibi SPECT at West China Hospital from May 2019 to April 2021. Normal and abnormal scans were selected from both stress and rest tests based on the report system. Due to missing data, not all patients had paired stress and rest scans. However, all individual studies included NAC images, CTAC images, and paired low-dose CT images.

Patient preparation

Patients are required to fast for at least 4 h prior to the examination. Cardiac medications, including calcium channel blockers and β-blockers, should be withheld on the day of the study. Additionally, patients should refrain from consuming strong tea, coffee, or other caffeine-containing beverages, as well as methylxanthine-containing medications, for at least 12 h before pharmacologic stress imaging. All radiopaque objects in the thoracic region should be removed prior to imaging [24, 25].

Imaging acquisition and processing

All rest/stress cardiac SPECT images were obtained using a dual-head integrated SPECT/CT camera (GE Discovery NM/CT 670) with an electrocardiographically (ECG)-gated two-day imaging protocol. Both rest and stress SPECT images were gated at 8 frames per cardiac cycle. SPECT images were acquired using a low-energy high-resolution (LEHR) collimator to optimize resolution, with a 20% energy window centered on the 140 keV photopeak of ^{99m}Tc. Approximately 60 min after the injection of 740 MBq 99mTc-sestamibi, SPECT images were acquired with a 180° orbit from right anterior oblique (RAO) to left posterior oblique (LPO). The scan speed was 20 s per projection, with a 3° rotation per cycle for both the rest and stress studies. A low-dose CT scan was acquired after the rest/stress SPECT acquisitions for attenuation correction (AC) with the following parameters: tube current: 20 mA, tube voltage: 120 kV, rotation time: 0.8 s, pitch: 0.938, number of slices: 30, and slice thickness: 5 mm. The matrix size for both projections

and reconstructions was 64 × 64 pixels, with a pixel size of 6.8 × 6.8 mm.

All studies were processed using Myovation protocol and done on a Xeleris 4.0 (GE Healthcare) workstation. The 3D ordered subset maximization expectation algorithm (OSEM, 2 iterations and 10 subsets) was used in both NAC and CTAC images, and post-filtering was applied with Butterworth filter (cutoff frequency of 0.4 cycles/cm and power of 10). The CT-based attenuation maps were manually registered with the SPECT images using the scanner software (GE ACQC) if there was any mismatch. No scatter correction was applied for all SPECT images.

Pre-processing of images

The transverse NAC, CTAC, and low-dose CT images were resampled to a resolution of 64 × 64 × 32 using center cropping and zero-padding. During preprocessing, the voxel values of NAC, CTAC and low dose CT images were restricted to ranges of 0 to 1200, 0 to 3600, and 0 to 4800, respectively. All images' intensities values were normalized within the range from 0 to 1.

Architectures of feature alignment attenuation correction network

In this study, we proposed a feature alignment attenuation correction network (FA-ACNet) based on a conventional 3D U-Net framework [26]. The overview architecture of FA-ACNet is shown in Fig. 1.

During training, we added additional parallel branches in the downsampling process to handle two input types separately: one with only NAC SPECT as input, and the other with both NAC SPECT and CT as input simultaneously. These are fed into the SPECT encoder (Est) and the SPECT/CT encoder (Esc) respectively to obtain encoded multi-scale features, which are then fed separately into the decoder and feature alignment module (FAM). The feature alignment module (FAM) receives multi-scale features and outputs a binary classification indicating whether the multi-scale features originated from NAC SPECT and CT, or from NAC SPECT alone. Within the decoder, these multi-scale features are progressively merged into the network to produce the Deep AC images for both input schemes. It is important to note that while the two input feature types share a single decoder, they are processed independently during the forward pass, resulting in two separate outputs. During inference, only NAC SPECT is used as input, with the goal of achieving output comparable to the result from

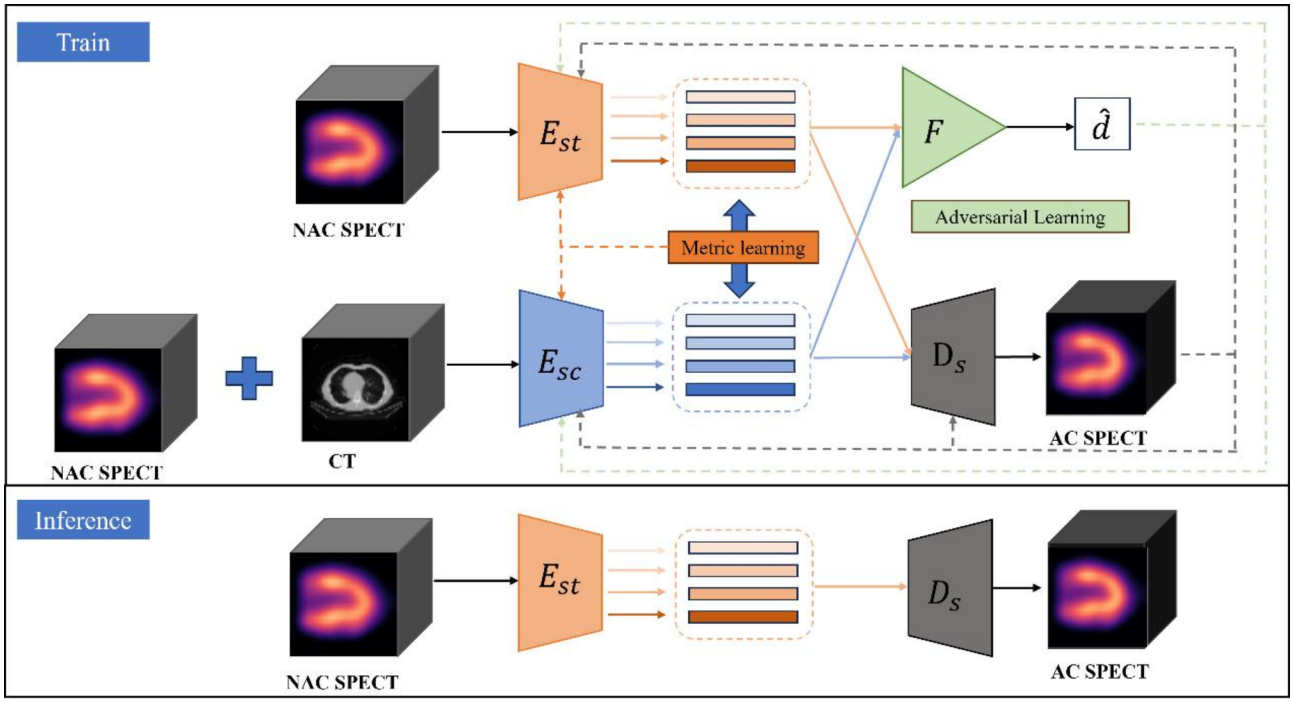

Fig. 1 Overview of the proposed FA-ACNet. The architecture of FA-ACNet consists of two encoders Est and Esc. Est receives only NAC SPECT images, while Esc receives both NAC SPECT and CT images simultaneously. The plus sign indicates concatenation in the channel dimension, i.e., concat operation. F denotes the Feature alignment module (FAM) which receives multi-scale features and outputs a binary classification ($\hat{d}$) indicating whether the multi-scale features originated from NAC SPECT and CT, or from NAC SPECT alone. Ds represents the decoder, which generates the predicted Deep AC images from NAC SPECT and CT, or from NAC SPECT alone

using both NAC SPECT and CT as input. Specifically, the input data passes through 5 alternately connected down-sampling convolution modules and 4 max pooling layers. Each down-sampling convolution module contains two sets of convolution layers, combined with ReLU activation function. Simultaneously, multi-scale features will also pass through 5 concatenated up-sampling convolution modules, which replace one convolution layer with a deconvolution layer based on the down-sampling convolution module. Metric learning and adversarial learning are employed to align the encoded features originated from NAC SPECT to those from NAC SPECT and CT. Detailed descriptions of these learning techniques are provided in the Supplementary Materials. The generator network in this paper minimizes the MSE loss using labeled data. The two loss functions are as follows:

$$\mathcal{L}_{mse} = \frac{1}{2n}\sum_{i=1}^{n}(\hat{y}_i^s - y_i)^2 + (\hat{y}_i^{sc} - y_i)^2 \tag{1}$$

$$\begin{aligned}\mathcal{L}_{mse} = {} & \tfrac{1}{2n}\sum_{i=1}^{n}((x_i + \hat{\mu}_i^s) - y_i)^2 \\ & +((x_i + \hat{\mu}_i^{sc}) - y_i)^2\end{aligned} \tag{2}$$

The first formula corresponds to the loss function for directly generating Deep AC from NAC SPECT. The second formula is used when generating Deep AC indirectly from NAC SPECT. The x^s, (x^s, x^c), $y^s$and y^{sc} denote the original NAC SPECT, the NAC SPECT and CT, and the corresponding output Deep AC, respectively.

Network training parameters

FA-ACNet was trained using 5-fold cross-validation and tested on an independent internal testing set, with paired input (NAC) and output (Deep AC) images. The final learning rate of 0.00002 and the batch size of 16 were determined through experience and grid search. The FA-ACNet was trained for 5000 epochs optimized by Adam [27] for the whole model except the feature alignment module which adopted stochastic gradient descent (SGD) optimizer [28]. We use the early stopping technique and have a patience setting of 200. In the total loss function of FA-ACNet, the weight coefficients of loss function of adversarial learning and distance metric learning were set to 0.5 and 2, respectively, and the discriminator's parameters were updated every three epochs. The model was implemented using the PyTorch framework [29]. Model training and testing were performed on an Ubuntu server with four Tesla P100 (NVIDIA) graphics processing unit and 64GB RAM.

Imaging quality evaluation for deep AC

The voxel-wise performance of FA-ACNet was evaluated by comparing it with the CTAC. The index quantified included mean square error (MSE), peak signal-to-noise ratio (PSNR) and structural similarity (SSIM). MSE is a common estimator for image quality, defined as:

$$\begin{aligned}MSE = {} & \tfrac{1}{mnc} \\ & \sum_{i=1}^{m}\sum_{j=1}^{n}\sum_{k=1}^{c}[\hat{y}(i,j,k) - y(i,j,k)]^2\end{aligned} \tag{3}$$

where $\widehat{y}$ and y represent the Deep AC and the original CTAC, respectively.

The well-known PSNR is defined as:

$$PSNR = 10 \cdot \log_{10}(\frac{MAX^2}{MSE}) \tag{4}$$

where MAX is the maximum possible pixel value, in our study, the value is 1. Additionally, the SSIM index is calculated as:

$$SSIM = \frac{(2\mu_x\mu_y + c_1)(2\sigma_{xy} + c_2)}{(\mu_x{}^2 + \mu_y{}^2 + c_1)(\sigma_x{}^2 + \sigma_y{}^2 + c_2)} \tag{5}$$

where μ and σ denote the average and the standard deviation of the original image x and the test image y. σ_{xy} is the covariance of x and y. The two variables c_1 and c_2 are constants that prevent numerical instabilities.

Clinical evaluation of SSS/SRS for Deep AC

Moreover, the summed stress scores (SSS) and summed rest scores (SRS) for all generated Deep AC images were evaluated and compared to the CTAC images' results. Visual semi-quantitative interpretation was assessed using 17-segment, 5-point scoring system (0 = normal, 4 = absent tracer uptake) by an independent nuclear medicine physician. Totally, An SSS/SRS below 4 is considered normal or minimally abnormal, scores between 4 and 8 indicate mild abnormalities, scores between 9 and 13 suggest moderate abnormalities, and scores of 13 or more suggest significant extensive ischemia [30].

Statistical analysis

The paired t test was performed to determine whether the MSE, SSIM and PSNR were significantly different between baseline U-Net and FA-ACNet. The Mann-Whitney U test was performed to compare the performance of FA-ACNet in different subgroups. The Bland-Altman plot was used to evaluation the difference of clinical metrics between Deep AC and CTAC images. All analyses were conducted using MedCalc® statistical software. P values less than 0.05 were considered statistically significant.

Table 1 Clinical characteristics of 202 subjects

Characteristic	Overall ($n=202$)	Training set ($n=167$)	Testing set ($n=35$)
Age (year)	65.40 ± 11.0	64.05 ± 17.54	57.7 ± 11.4
Gender			
Male	94 (46.53)	71 (42.52)	23 (65.71)
Female	108 (53.47)	96 (57.48)	12 (34.29)
BMI (kg/m^2)	25.30 ± 2.93	25.27 ± 3.07	25.30 ± 2.16
Past medical history			
Diabetes mellitus	36 (17.82)	30 (17.96)	6 (17.14)
Hypertension	97 (48.02)	81 (48.50)	16 (45.71)
Dyslipidemia	36 (17.82)	22 (13.17)	14 (40.00)
History of CAD	48 (23.76)	21 (12.57)	27 (77.14)
Imaging type			
Stress	86 (42.57)	69 (41.32)	17 (48.57)
Rest	116 (57.43)	98 (58.68)	18 (51.43)
Imaging interpretation			
Normal or minimal abnormality	140 (69.31)	107 (64.07)	33 (94.29)
Mild abnormality	49 (24.26)	47 (28.14)	2 (5.17)
Moderate abnormality	9 (4.46)	9 (5.39)	0 (0.00)
Significant abnormality	4 (1.98)	4 (2.40)	0 (0.00)

Qualitative data are expressed as numbers followed by percentages in parentheses; continuous data are expressed as mean ± SD. BMI, body mass index; CAD, coronary artery disease

Results

We collected 202 clinical myocardial perfusion SPECT examinations for training ($n=167$) and testing ($n=35$) the model. The clinical characteristics of the patients enrolled in the study, such as age, gender, body mass index (BMI), and past medical history, are summarized in Table 1. According to the imaging interpretation results from the radiological information system, 69.31% of the studies were classified as normal or minimally abnormal, with no evidence of myocardial ischemia.

Performance of FA-ACNet for CT-free attenuation correction

The results of indirect and direct methods to for generating Deep AC from NAC are shown in Table 2. After 5-fold cross validation, the performance was evaluated in terms of averaged MSE (10^{-6}), SSIM and PSNR, compared with the ground-truth CTAC. For the indirect prediction of Deep AC, the FA-ACNet showed improved MSE and PSNR compared to the baseline, with values of 16.94 ± 2.03 and 43.73 ± 0.50, respectively (both $P<0.05$). There was no significant difference in the SSIM, although the SSIM values for both methods exceeded 0.9. This indicates that incorporating anatomical CT features significantly improved CT-free AC performance compared to the baseline. For the direct prediction of Deep AC, FA-ACNet demonstrated a notable improvement in SSIM, which increased from 0.3655 ± 0.0084 to 0.9717 ± 0.0002 ($P<0.05$). However, the MSE and PSNR did not show significant improvement. Overall, FA-ACNet performed better in generating Deep AC indirectly than directly, as reflected in all three metrics. Figures 2 and 3 display two case examples in horizontal long axis (HLA), vertical long axis (VLA), and short axis (SA) views, showing the NAC, CTAC, and Deep AC images. Following CT-free AC, the Deep AC images demonstrated greater consistency with the CTAC images, in contrast to the NAC images.

In the subsequent ablation study on indirect prediction of Deep AC from NAC, the results in Table 3 show a significant decrease in CT-free AC performance when the decoder was shared without feature alignment. The MSE increased from 25.46 ± 2.78 to 27.83 ± 2.99. However, when either adversarial learning or distance metric learning was used to align multi-scale features, the performance of CT-free AC improved compared to the baseline. The integrated FA-ACNet model achieved the best results, with an MSE of 16.94 ± 2.03, a PSNR of 43.73 ± 0.50, and an SSIM of 0.9955 ± 0.0006.

In the further independent internal testing on 35 cardiac SPECT studies, we utilized the best-performing model from the five-fold cross-validation experiments, the FA-ACNet achieved an MSE of 11.98, a PSNR of 45.54, and an SSIM of 0.9976.

We further categorized all studies into various subgroups, including gender, imaging type (stress vs. rest), imaging interpretation (normal vs. abnormal), as well as non-obesity (BMI <28) and obesity (BMI ≥ 28) groups. As shown in Table 4, FA-ACNet for CT-free AC achieved higher image quality in the male group than in the female group, reflected by lower MSE values (14.81 ± 3.34 vs. 18.68 ± 3.83, $P=0.01$) in the training set. No statistically significant differences were observed across imaging types ($P=0.07$), interpretation results ($P=0.09$), or BMI groups ($P=0.70$). Additionally, SSIM and PSNR metrics showed minimal variations across these subgroups. In the testing set, as shown in Table 5, no statistically

Table 2 Five-fold cross-validation results of U-Net and FA-ACNet for indirect and direct prediction of deep AC from NAC images

Method	Indirect prediction of Deep AC			Direct prediction of Deep AC		
	MSE (10^{-6})	SSIM	PSNR	MSE (10^{-6})	SSIM	PSNR
Baseline: U-Net	25.46 ± 2.78	0.9927 ± 0.0021	42.16 ± 0.54	142.42 ± 2.73	0.3655 ± 0.0084	33.65 ± 0.29*
FA-ACNet	**16.94 ± 2.03***	**0.9955 ± 0.0006**	**43.73 ± 0.50***	879.38 ± 28.71*	0.9717 ± 0.0002*	31.44 ± 0.08

The group generating the best result is bolded

* This indicates that the index was significantly different between baseline U-Net and FA-ACNet ($P<0.05$)

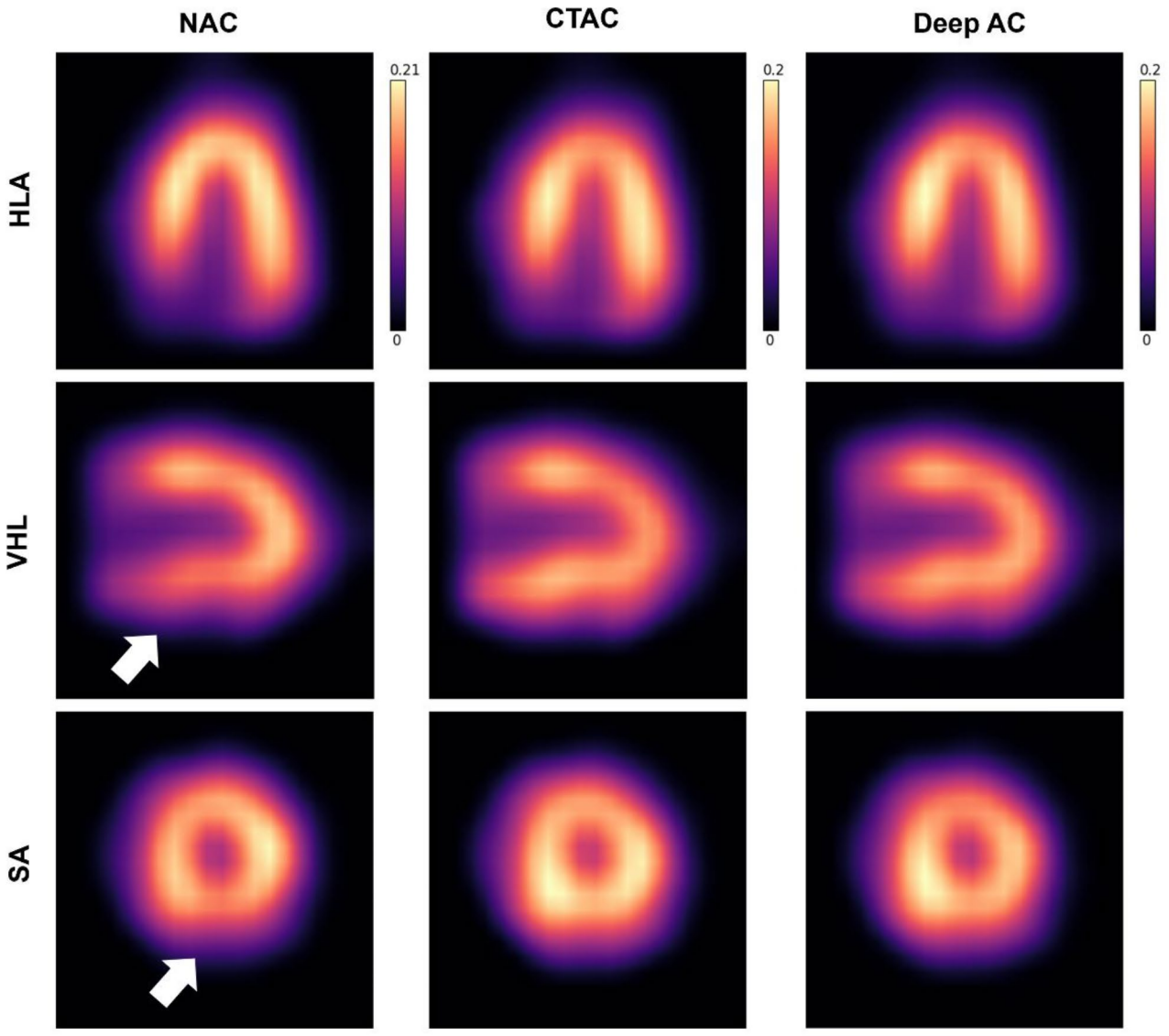

Fig. 2 Rest NAC, CTAC, and DeepAC images from a 55-y-old man with body mass index of 27.53. On vertical long-axis images (middle) and short-axis images (bottom), there were defects in the inferior wall on NAC images only (white arrows). After AC correction, the CTAC and Deep AC images were both normal without defects. The MSE and SSIM was 74.9×10^{-6} and 0.9992 between Deep AC and CTAC images

significant differences were observed across all different subgroups.

Clinical evaluation of SSS/SRS for Deep AC

The comparison of SSS or SRS between Deep AC and CTAC is illustrated in Fig. 4. In the training set, the mean difference of SSS/SRS value was 0.2 and the 95% LoAs ranging from − 2.3 to 2.8. In the testing set, the mean difference of SSS/SRS value was 0.1, and the 95% LoAs ranging from − 1.9 to 2.1.

When assessing global perfusion scores in the training set, 8 out of 167 studies (4.79%) showed changes in perfusion categories. 4 studies changed from normal perfusion (SSS = 0, SRS = 0, SSS = 0 and SRS = 0, respectively) to mildly abnormal perfusion (SSS = 4, SRS = 4 SSS = 4 and SRS = 4, respectively), 3 studies changed from mildly abnormal perfusion (SRS = 4, SSS = 4 and SRS = 4, respectively) to normal perfusion (SRS = 1, SSS = 2 and SRS = 2, respectively), and the other one changed from mildly abnormal perfusion(SSS = 8) to moderately abnormal perfusion (SSS = 10). In the testing set, 2 out of 35 studies (5.71%) showed changes in perfusion categories. One changed from minimal abnormal perfusion (SRS = 3) to mildly abnormal perfusion (SRS = 4), and the other one changed from mildly abnormal perfusion (SSS = 5) to moderately abnormal perfusion (SSS = 9).

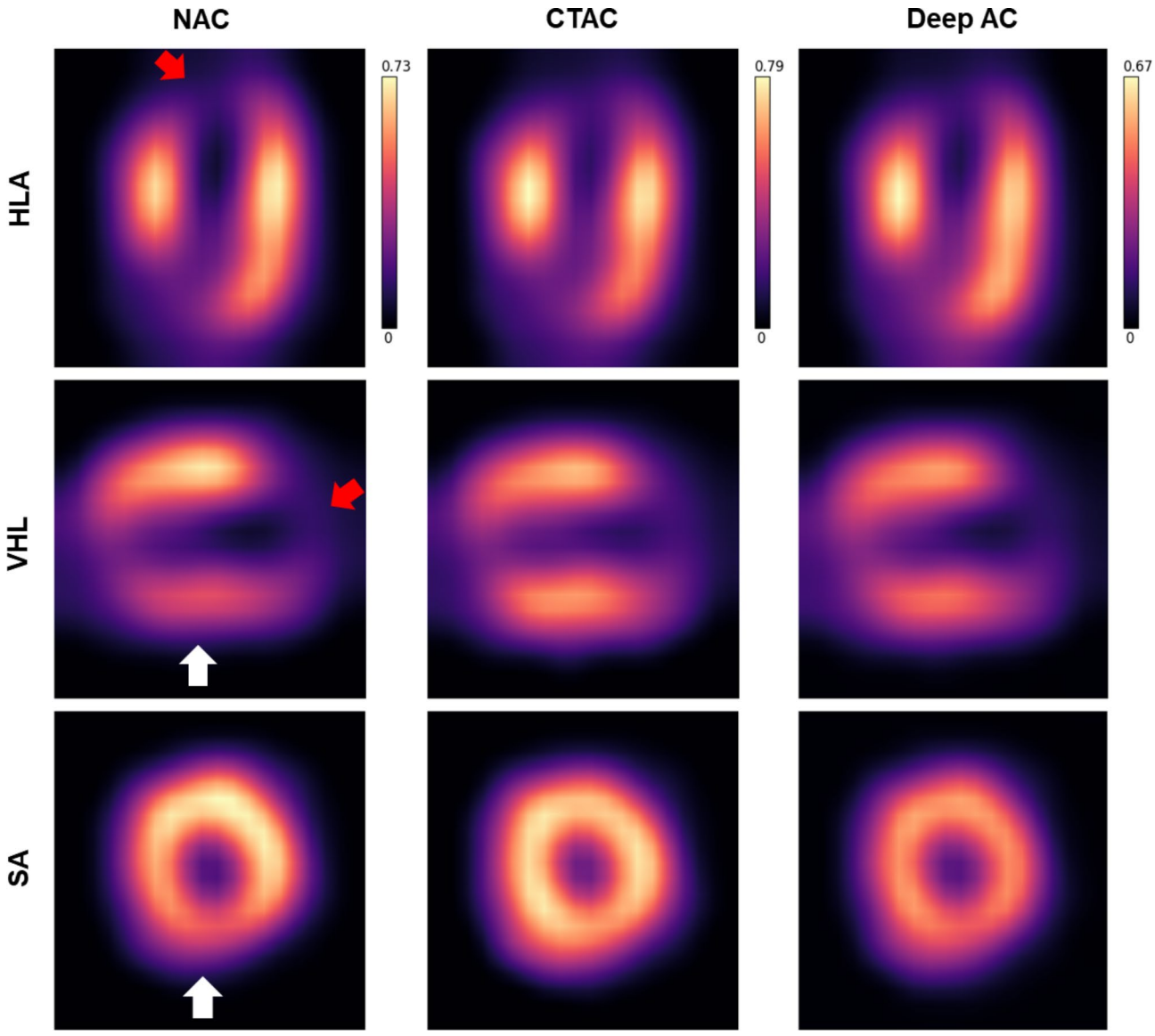

Fig. 3 Rest NAC, CTAC, and DeepAC images from an 83-y-old woman with body mass index of 25.77. On horizontal long-axis (top), vertical long-axis images (middle) and short-axis images (bottom), there were defects in the apex, anterior (red arrows) and inferior walls (white arrows) on NAC images. After AC correction, the CTAC and Deep AC images were still abnormal. The MSE and SSIM was 204.54×10^{-6} and 0.9926 between Deep AC and CTAC images

Table 3 Results of ablation study on FA-ACNet for indirect prediction of deep AC from NAC images

Method	Adversarial learning	Metric learning	MSE (10^{-6})	SSIM	PSNR
Baseline: U-Net	—	—	25.46 ± 2.78	0.9927 ± 0.0021	42.16 ± 0.54
Direct shared decoder	—	—	27.83 ± 2.99	0.9936 ± 0.0006	41.93 ± 0.55
FA-ACNet	√	—	21.76 ± 3.58	0.9948 ± 0.0006	42.98 ± 0.62
FA-ACNet	—	√	18.82 ± 2.18	0.9951 ± 0.0003	43.09 ± 0.28
FA-ACNet	√	√	**16.94 ± 2.03**	**0.9955 ± 0.0006**	**43.73 ± 0.50**

The group generating the best result is bolded

Discussion

We proposed a novel DL-based CT-free AC approach for cardiac SPECT. Evaluation using 202 clinical studies showed that FA-ACNet can generate Deep AC images that are consistent with CTAC. This advancement is particularly beneficial for clinical applications involving SPECT-only scanners, where CT scans are typically unavailable. The ability to produce high-quality AC images without the need for CT scans not only reduces

Table 4 Performance of FA-ACNet for predicting Deep AC from NAC across different subgroups in the training set

	MSE (10^{-6})	SSIM	PSNR
Training set(*n* = 167)	16.94 ± 2.03	0.9955 ± 0.0006	43.73 ± 0.50
Imaging type			
Stress (*n* = 69)	18.77 ± 2.84	0.9950 ± 0.0054	43.32 ± 3.45
Rest (*n* = 98)	16.44 ± 4.19	0.9958 ± 0.0044	44.02 ± 2.93
Imaging interpretation			
Normal (*n* = 107)	15.96 ± 1.39	0.9960 ± 0.0045	44.20 ± 2.89
Abnormal (*n* = 60)	18.55 ± 4.22	0.9945 ± 0.0053	42.90 ± 3.48
Gender			
Male (*n* = 71)	14.81 ± 3.34*	0.9946 ± 0.0057	43.08 ± 3.00
Female (*n* = 96)	18.68 ± 3.83	0.9961 ± 0.0041	44.22 ± 3.21
BMI (kg/m^2)			
BMI ≥ 28 (*n* = 29)	16.02 ± 3.67	0.9956 ± 0.0041	42.88 ± 3.06
BMI<28 (*n* = 138)	17.11 ± 2.82	0.9954 ± 0.0050	43.91 ± 3.17

BMI, body mass index; * This indicates that the MSE was significantly different between male and female group ($P < 0.05$)

Table 5 Performance of FA-ACNet for predicting Deep AC from NAC across different subgroups in the testing set

	MSE (10^{-6})	SSIM	PSNR
Testing set (*n* = 35)	11.98	0.9976	45.54
Imaging type			
Stress (*n* = 17)	12.80	0.9975	45.62
Rest (*n* = 18)	11.20	0.9976	45.46
Imaging interpretation			
Normal (*n* = 33)	11.94	0.9975	45.56
Abnormal (*n* = 2)	12.54	0.9981	45.15
Gender			
Male (*n* = 23)	11.98	0.9975	45.24
Female (*n* = 12)	11.97	0.9976	46.10
BMI (kg/m^2)			
BMI ≥ 28 (*n* = 2)	11.99	0.9965	45.43
BMI<28 (*n* = 33)	11.98	0.9976	45.54

BMI, body mass index

patient radiation exposure but also enhances accessibility for facilities that rely solely on SPECT imaging.

In our study, we enhanced CT-free AC performance by incorporating CT features. This multi-scale feature alignment significantly improved the MSE and PSNR, suggesting that FA-ACNet effectively aligns features between CT-based and CT-free AC tasks. This alignment enables better pixel-wise feature embedding, enhancing the accuracy of CT-free AC predictions. Additionally, we investigated both direct and indirect approaches to generating Deep AC images. Similar with Chen et al. [4], our results indicate that the indirect approach, which predicts voxel differences between NAC and CTAC images, outperformed the direct method in terms of MSE. Remarkably, our indirect method does not rely on generating attenuation maps.

In the subgroup analysis, imaging type, myocardial perfusion categories, and BMI did not significantly influence performance in the training test. However, a higher bias in female subjects was observed compared to male subjects, consistent with findings from Shi et al. [23]. This discrepancy may stem from anatomical differences between genders. Future studies should aim to include a larger cohort of female patients, encompassing a wide range of breast sizes and densities, to further assess the model's performance in this group.

Semi-quantitative evaluation of myocardial perfusion using Deep AC showed strong agreement with CTAC in most studies. In the training set, the bias and 95% limits of agreement (LoAs) for SSS/SRS were 0.2 and [-2.3, 2.8], respectively. In the internal testing set, the bias was 0.1, with 95% LoAs of [-1.9, 2.1]. However, 4.79% of studies in the training set and 5.71% in the testing set showed shifts in their global perfusion categories, which is higher than the 3% reported by Prieto et al. [22]. These changes were mostly observed in studies near the categorical boundaries. Additionally, since visual analysis is subjective and prone to inter- and intra-observer variability, quantitative metrics like total perfusion deficit (TPD) may offer more reliable assessments [31]. This variability could influence clinical decision-making. It is crucial that Deep AC images should be carefully reviewed by nuclear cardiology physicians before being used for clinical interpretation.

While we did not directly compare our method with previous studies, our approach provides a new perspective on DL-based CT-free AC for cardiac SPECT. Earlier studies have focused on the types of inputs used in CT-free AC, whether for transforming NAC images into AC images or for generating attenuation maps. For example, Chen X et al. proposed a customized 3D dual squeeze-and-excitation residual dense network for CT-free AC, incorporating additional data like BMI, gender, and scatter-window data to improve network performance [32]. Similarly, Chen Y et al. developed a DL model to predict attenuation maps from NAC images using both photopeak window and varied scatter window settings from NAC images as inputs [33]. In contrast, our study investigates the added value of incorporating CT features in intermediate steps, showing that multi-scale features derived from the NAC SPECT and CT significantly enhance the CT-free AC performance, offering a promising alternative for future DL-based AC strategies.

Despite these strengths, there are several limitations. Firstly, this is a single-center study and all the cardiac SPECT images were obtained using ^{99m}Tc-Sestamibi imaging and a single scanner. The performance of FA-ACNet for different tracers (such as ^{99m}Tc-Tetrofosmin), different cameras, different image acquisition or processing protocols, or different patient populations needs to be further validated. Secondly, our study did not use paired rest and stress scans, which would have allowed

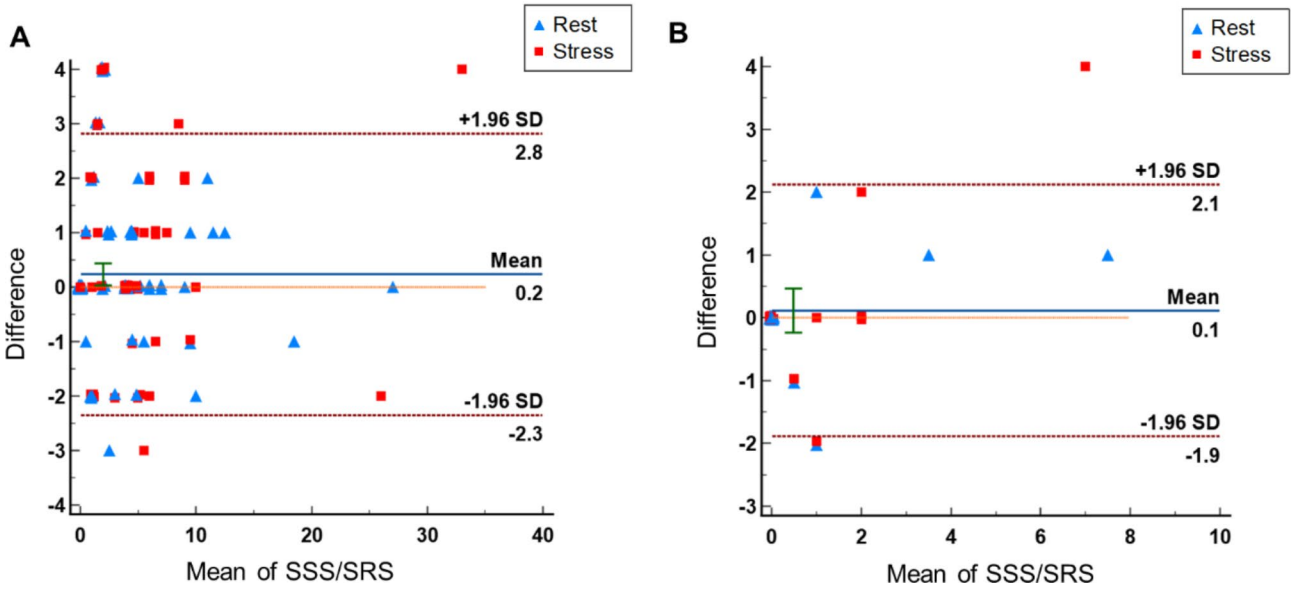

Fig. 4 Bland-Altman plots of SSS/SRS values between Deep AC and CTAC in the training set (**A**) and testing set (**B**). The dotted lines represent the 95% limits of agreement (LoAs)

us to train the model on images with defects and validate it on normal images. Finally, the implications of this CT-free AC approach on cardiac dedicated SPECT scanners, which have a limited field-of-view, should be further explored. Although we implemented automated quality assessment steps using GE ACQC software to correct any mismatch between NAC images and attenuation maps, there is still the possibility that the model may have learned artifacts present in the CTAC images, particularly if a significant portion of the data contained such artifacts.

Conclusion

We proposed a novel DL-based CT-free AC approach for cardiac SPECT that has the potential to generate AC images without the need for a CT scan. This approach can reduce radiation exposure to patients and accelerate the preprocessing steps of cardiac SPECT in clinical workflows. Preliminary results demonstrated that incorporating multi-scale features derived from NAC SPECT and CT significantly enhances CT-free AC performance compared to the baseline U-Net model. This offers a new perspective on improving CT-free AC for cardiac SPECT.

Abbreviations

MPI	Myocardial perfusion imaging
SPECT	Single-photon emission computed tomography
CAD	Coronary artery disease
ICA	Invasive coronary angiography
AC	Attenuation correction
DL	Deep learning
NAC	Non-attenuation-corrected
FAM	Feature alignment module
ECG	Electrocardiographically
LEHR	Low-energy high-resolution
RAO	Right anterior oblique
LPO	Left posterior oblique
OSEM	Ordered subset maximization expectation algorithm
FA-ACNet	Feature alignment attenuation correction network
MSE	Mean square error
ReLU	Rectified linear unit
MMD	Maximum mean discrepancy
CORAL	Correlation alignment
PSNR	Peak signal-to-noise ratio
SSIM	Structural similarity
BMI	Body mass index

Supplementary Information

The online version contains supplementary material available at https://doi.org/10.1186/s12880-025-01570-y.

Supplementary Material 1

Supplementary Material 2

Acknowledgements

This project was financially supported by the 1.3.5 project for disciplines of excellence, West China Hospital, Sichuan University (ZYGD23016 & 2021HXFH033), Sichuan Science and Technology Program under Grant 2022ZDZX0023, and Key Projects of the National Natural Science Foundation of China (92359204).

Author contributions

All authors contribute to the study's conception and design. Conception and design of the study: PY, ZZ, QG and ZZ; Data acquisition: PY, JW, LJ, LY and HC; Neural network implementation and code writing: ZZ, JW and GQ; Image reconstruction: PY, LJ, LY, HC and LL; Image analysis: PY, ZZ, and LL; Clinical evaluation: PY, ZZ, and LL. Writing of the first draft of the manuscript: PY. All authors commented on previous versions of the manuscript. All authors read and approved the final manuscript.

Funding

This study has received funding by the 1.3.5 project for disciplines of excellence, West China Hospital, Sichuan University (ZYGD23016&2021HXFH033), Sichuan Science and Technology Program

under Grant 2022ZDZX0023, and Key Projects of the National Natural Science Foundation of China (92359204).

Data availability
The datasets generated and analyzed during the current study are not publicly available but available from the corresponding author upon reasonable request.

Declarations

Ethics approval and consent to participate
The study was performed in accordance with the Declaration of Helsinki and approved by the Institutional Ethics Committee of West China Hospital in Sichuan University (approval number: 20231386). The retrospective data collection has obtained the waiver of consent form by the ethics committee.

Consent for publication
Not applicable.

Competing interests
The authors declare no competing interests.

Received: 26 July 2024 / Accepted: 22 January 2025
Published online: 04 February 2025

References

1. Loong CY, Anagnostopoulos C. Diagnosis of coronary artery disease by radionuclide myocardial perfusion imaging. Heart. 2004;90(Suppl 5):v2–9.
2. Beller GA. Radionuclide perfusion imaging techniques for evaluation of patients with known or suspected coronary artery disease. Adv Intern Med. 1997;42:139–201.
3. Taqueti VR, Di Carli MF. Radionuclide myocardial perfusion imaging for the evaluation of patients with known or suspected coronary artery disease in the era of multimodality cardiovascular imaging. Prog Cardiovasc Dis. 2015;57(6):644–53.
4. Chen X, Zhou B, Xie H, Shi L, Liu H, Holler W, Lin M, Liu YH, Miller EJ, Sinusas AJ, et al. Direct and indirect strategies of deep-learning-based attenuation correction for general purpose and dedicated cardiac SPECT. Eur J Nucl Med Mol Imaging. 2022;49(9):3046–60.
5. Singh B, Bateman TM, Case JA, Heller G. Attenuation artifact, attenuation correction, and the future of myocardial perfusion SPECT. J Nuclear Cardiology: Official Publication Am Soc Nuclear Cardiol. 2007;14(2):153–64.
6. Parker MW, Iskandar A, Limone B, Perugini A, Kim H, Jones C, Calamari B, Coleman CI, Heller GV. Diagnostic accuracy of cardiac positron emission tomography versus single photon emission computed tomography for coronary artery disease: a bivariate meta-analysis. Circulation Cardiovasc Imaging. 2012;5(6):700–7.
7. Boz A, Yildiz A, Güngör F, Karayalçin B, Erkiliç M. The volume effect of the stomach on intestinal activity on same-day exercise–rest Tc-99m tetrofosmin myocardial imaging. Clin Nucl Med. 2001;26(7):622–5.
8. Patton JA, Turkington TG. SPECT/CT physical principles and attenuation correction. J Nucl Med Technol. 2008;36(1):1–10.
9. Heller GV, Links J, Bateman TM, Ziffer JA, Ficaro E, Cohen MC, Hendel RC. American Society of Nuclear Cardiology and Society of Nuclear Medicine joint position statement: attenuation correction of myocardial perfusion SPECT scintigraphy. J Nuclear Cardiology: Official Publication Am Soc Nuclear Cardiol. 2004;11(2):229–30.
10. Wolak A, Slomka PJ, Fish MB, Lorenzo S, Berman DS, Germano G. Quantitative diagnostic performance of myocardial perfusion SPECT with attenuation correction in women. J Nuclear Medicine: Official Publication Soc Nuclear Med. 2008;49(6):915–22.
11. Barrett JF, Keat N. Artifacts in CT: recognition and avoidance. Radiographics: Rev Publication Radiological Soc North Am Inc. 2004;24(6):1679–91.
12. Goetze S, Wahl RL. Prevalence of misregistration between SPECT and CT for attenuation-corrected myocardial perfusion SPECT. J Nuclear Cardiology: Official Publication Am Soc Nuclear Cardiol. 2007;14(2):200–6.
13. Goetze S, Brown TL, Lavely WC, Zhang Z, Bengel FM. Attenuation correction in myocardial perfusion SPECT/CT: effects of misregistration and value of reregistration. J Nuclear Medicine: Official Publication Soc Nuclear Med. 2007;48(7):1090–5.
14. Bockisch A, Freudenberg LS, Schmidt D, Kuwert T. Hybrid imaging by SPECT/CT and PET/CT: proven outcomes in cancer imaging. Semin Nucl Med. 2009;39(4):276–89.
15. Akhtar Y, Dakua SP, Abdalla A, Aboumarzouk OM, Ansari MY, Abinahed J, Elakkad MSM, Al-Ansari A. Risk assessment of computer-aided diagnostic software for hepatic resection. IEEE Trans Radiation Plasma Med Sci. 2021;6(6):667–77.
16. Ansari MY, Mangalote IAC, Meher PK, Aboumarzouk O, Al-Ansari A, Halabi O, Dakua SP. Advancements in Deep Learning for B-Mode Ultrasound Segmentation: a Comprehensive Review. IEEE Trans Emerg Top Comput Intell 2024.
17. Ansari MY, Qaraqe M, Righetti R, Serpedin E, Qaraqe K. Unveiling the future of breast cancer assessment: a critical review on generative adversarial networks in elastography ultrasound. Front Oncol. 2023;13:1282536.
18. Chen X, Liu C. Deep-learning-based methods of attenuation correction for SPECT and PET. J Nuclear Cardiology: Official Publication Am Soc Nuclear Cardiol. 2023;30(5):1859–78.
19. Yang J, Shi L, Wang R, Miller EJ, Sinusas AJ, Liu C, Gullberg GT, Seo Y. Direct attenuation correction using deep learning for Cardiac SPECT: a feasibility study. J Nuclear Medicine: Official Publication Soc Nuclear Med. 2021;62(11):1645–52.
20. Nguyen TT, Chi TN, Hoang MD, Thai HN, Duc TN. 3D Unet Generative Adversarial Network for Attenuation Correction of SPECT Images. In: 2020 *4th International Conference on Recent Advances in Signal Processing, Telecommunications & Computing (SigTelCom): 28–29 Aug. 2020 2020*; 2020: 93–97.
21. Shanbhag AD, Miller RJH, Pieszko K, Lemley M, Kavanagh P, Feher A, Miller EJ, Sinusas AJ, Kaufmann PA, Han D, et al. Deep learning–based attenuation correction improves diagnostic accuracy of Cardiac SPECT. J Nuclear Medicine: Official Publication Soc Nuclear Med. 2023;64(3):472–8.
22. Prieto Canalejo MA, Palau San Pedro A, Geronazzo R, Minsky DM, Juárez-Orozco LE, Namías M. Synthetic Attenuation Correction Maps for SPECT Imaging Using Deep Learning: A Study on Myocardial Perfusion Imaging. *Diagnostics (Basel, Switzerland)* 2023, 13(13).
23. Shi L, Onofrey JA, Liu H, Liu YH, Liu C. Deep learning-based attenuation map generation for myocardial perfusion SPECT. Eur J Nucl Med Mol Imaging. 2020;47(10):2383–95.
24. Strauss HW, Miller DD, Wittry MD, Cerqueira MD, Garcia EV, Iskandrian AS, Schelbert HR, Wackers FJ, Balon HR, Lang O, et al. Procedure guideline for myocardial perfusion imaging 3.3. J Nucl Med Technol. 2008;36(3):155–61.
25. Fathala A. Myocardial perfusion scintigraphy: techniques, interpretation, indications and reporting. Ann Saudi Med. 2011;31(6):625–34.
26. Ronneberger O, Fischer P, Brox T. U-Net: Convolutional Networks for Biomedical Image Segmentation. In: 2015; Cham. Springer International Publishing; 2015. pp. 234–41.
27. Kingma DP, Ba J. Adam: A Method for Stochastic Optimization. *arXiv: Learning* 2014.
28. Keskar NS, Socher R. Improving generalization performance by switching from adam to Sgd. arXiv Preprint arXiv:07628 2017.
29. Paszke A, Gross S, Massa F, Lerer A, Bradbury J, Chanan G, Killeen T, Zeming L, Gimelshein N, Antiga L et al. PyTorch: An Imperative Style, High-Performance Deep Learning Library arXiv. *arXiv* 2019:12 pp.-12 pp.
30. Czaja M, Wygoda Z, Duszańska A, Szczerba D, Głowacki J, Gąsior M, Wasilewski JP. Interpreting myocardial perfusion scintigraphy using single-photon emission computed tomography. Part 1. Kardiochirurgia I Torakochirurgia Polska = Pol J cardio-thoracic Surg. 2017;14(3):192–9.
31. Berman DS, Kang X, Gransar H, Gerlach J, Friedman JD, Hayes SW, Thomson LE, Hachamovitch R, Shaw LJ, Slomka PJ, et al. Quantitative assessment of myocardial perfusion abnormality on SPECT myocardial perfusion imaging is more reproducible than expert visual analysis. J Nuclear Cardiology: Official Publication Am Soc Nuclear Cardiol. 2009;16(1):45–53.
32. Chen X, Zhou B, Shi L, Liu H, Pang Y, Wang R, Miller EJ, Sinusas AJ, Liu C. CT-free attenuation correction for dedicated cardiac SPECT using a 3D dual squeeze-and-excitation residual dense network. J Nuclear Cardiology: Official Publication Am Soc Nuclear Cardiol. 2022;29(5):2235–50.

33. Chen Y, Pretorius PH, Yang Y, King MA, Lindsay C. Investigation of scatter energy window width and count levels for deep learning-based attenuation map estimation in cardiac SPECT/CT imaging. Phys Med Biol 2024.

Publisher's note